Solar Energy Materials & Solar Cells 307 (2026) 114658

Contents lists available at ScienceDirect

Solar Energy Materials and Solar Cells

journal homepage: www.elsevier.com/locate/solmat

Modification of the CZTS/CdS interface by introducing an intermediate CeO_2 layer

K. Timmo *, M. Pilvet, M. Danilson, V. Mikli, J. Krustok, A. Dolski, A. Nasyori, S. Bereznev, M. Grossberg-Kuusk, M. Kauk-Kuusik

Department of Materials and Environmental Technology, Tallinn University of Technology, Ehitajate tee 5, Tallinn, 19086, Estonia

ARTICLE INFO

Keywords:
CZTS solar cells
Kesterite
CeO_2
Hole-blocking layer
Intermediate layer

ABSTRACT

An ultrathin CeO_2 intermediate layer was introduced at the hetero-interface between the *p*-type Cu_2ZnSnS_4 (CZTS) absorber and the *n*-type CdS buffer to enhance carrier collection and overall device performance by hindering hole tunneling in kesterite thin-film solar cells. The CeO_2 layer was deposited by chemical bath deposition and pulsed laser deposition (PLD), and the impact of these deposition methods on the structural and compositional properties was systematically investigated. XPS and SEM/EDX analyses revealed that PLD suppresses Ce_2O_3 formation and enables precise control of the thickness of the CeO_2 layer. The optimized (<5 nm) CeO_2 interlayer was integrated into two different solar cell architectures: monograin layer solar cells and thin-film solar cells, resulting in enhanced device performance. The power conversion efficiency increased from 7.1% to 9.0% for monograin layer cells and from 4.5% to 6.7% for thin-film devices.

1. Introduction

Kesterite materials, $Cu_2ZnSn(S,Se)_4$ (CZTSSe), are quaternary chalcogenide semiconductors used as absorber layers in thin-film solar cells. They are attractive due to their composition based on earth-abundant, relatively low-toxicity elements, together with a direct, composition-tunable band gap of about 1.0–1.5 eV and absorption coefficients above $10^4\,cm^{-1}$, enabling efficient light harvesting in thin films [1,2]. For this reason, kesterites are widely regarded as a more sustainable alternative to conventional thin-film technologies such as $Cu(In,Ga)Se_2$ (CIGS) and CdTe. The mixed S/Se composition currently defines the state of the art, with certified CZTSSe efficiencies reaching 15.04% [3], while pure-sulfide Cu_2ZnSnS_4 (CZTS) has recently reached a certified efficiency of 11.96% [4]. Despite the attractive properties of the kesterite family, device performance remains limited by a pronounced V_{oc} deficit, reflecting substantial non-radiative recombination losses. These losses originate from the complex defect chemistry of kesterites as well as recombination pathways associated with both the absorber bulk and the heterojunction [5–7]. In pure-sulfide CZTS, such limitations are particularly severe at the absorber/buffer (CdS) interface, where a high density of surface and near-surface defects, together with non-ideal band alignment with CdS can enhance interfacial recombination and hinder efficient charge separation [8] [9].

The beneficial role of a thin wide-bandgap surface region was first identified in CIGS solar cells, where a Cu-poor ordered vacancy compound (OVC) formed at the absorber surface is considered to improve junction formation [10,11]. Due to its wider bandgap relative to the chalcopyrite bulk, this near-surface region can function as a hole-blocking layer, suppressing interfacial recombination while preserving efficient electron transport across the heterojunction [6,11,12]. Inspired by this concept, the insertion of an ultrathin wide-bandgap interlayer between CZTS and CdS has emerged as a widely investigated strategy to mitigate junction losses [13–15]. When properly engineered, this intermediate layer can simultaneously (i) passivate electrically active interface states, (ii) modify the interfacial electrostatics and band bending, and (iii) provide a selective energy barrier for holes, thereby suppressing interfacial recombination while preserving efficient electron extraction through tunnelling across the nanometre-scale layer [16–19]. More generally, properly engineered ultrathin interlayers can improve charge carrier collection by promoting selective carrier transport across the heterojunction. In this context, oxide interlayers are especially attractive due to their chemical stability, wide bandgaps (minimizing parasitic absorption), and compatibility with scalable deposition routes.

Among the investigated oxides, SnO_2 has been demonstrated as an effective ultrathin interfacial layer at the CZTS/CdS junction to improve

* Corresponding author.
E-mail address: kristi.timmo@taltech.ee (K. Timmo).

https://doi.org/10.1016/j.solmat.2026.114658
Received 21 May 2026; Received in revised form 18 August 2026; Accepted 19 August 2026

junction selectivity and suppress interfacial recombination [16]. This improvement is attributed to the combination of wide-bandgap passivation and favorable band alignment, where the oxide layer acts as a partial hole-blocking barrier while remaining sufficiently thin to avoid an excessive increase in series resistance. TiO_2 has also been investigated in kesterite solar cells, both as an ultrathin interfacial passivation layer and as an alternative electron-selective interface. These studies indicate that TiO_2 can improve the TiO_2/CZTSSe junction through more favorable energy-level alignment and reduced interface-related recombination. In devices using an ALD-deposited TiO_2 passivation layer, this has been reflected in a higher V_{oc} and an increased recombination activation energy extracted from temperature-dependent measurements [17,20].

A well-established interlayer material is Al_2O_3, which is well known in photovoltaics for its excellent surface passivation properties. In CZTS-based devices, ultrathin ALD-Al_2O_3 inserted at the absorber/buffer interface has been reported to reduce acceptor-like interface states, increase the depletion width, and suppress interfacial recombination [18] [21] [22,23]. Nevertheless, Al_2O_3 also highlights a general constraint of interlayer approaches: if the layer is too thick or highly insulating, or if it is chemically modified during subsequent CdS chemical bath deposition, it may introduce an additional transport barrier or increase series resistance that reduces the *FF* [18,22]. Therefore, most successful implementations require sub-nanometre to few-nanometre thickness control and careful integration with the buffer deposition process. Overall, prior studies on SnO_2, TiO_2 and Al_2O_3 interlayers demonstrate that ultrathin oxides can improve the absorber/buffer heterojunction through interface engineering, yielding enhanced charge carrier collection and improved photovoltaic performance [5,13,24].

Building on this concept, we introduce a CeO_2 interlayer at the CZTS/CdS interface. CeO_2 is a non-toxic, earth-abundant oxide with a wide bandgap (~ 3.2–3.6 eV), minimizing parasitic absorption [25,26]. Importantly, CeO_2 offers an excellent lattice match with CZTS (mismatch <0.4%), with lattice constants $a = b = 5.43$ Å [27], for CZTS and $a = b = 5.41$ Å for CeO_2 [26], which is expected to promote a high-quality, low-defect (potentially epitaxial) interface, thereby mitigating interface recombination. In addition to structural compatibility, the deeper valence band position of CeO_2 relative to CZTS is expected to provide an enhanced hole-blocking barrier. The valence band offset (VBO) at the CZTS/CeO_2 interface (~1.8-2.0 eV) is significantly larger than that of CZTS/CdS (~1.0-1.2 eV), which is expected to further suppress non-radiative recombination at the heterojunction and improve device performance [25,26,28,29]. Based on the literature values reported in these studies, the schematic energy band alignment of the proposed CZTS/CeO_2/CdS heterojunction, highlighting the hole-blocking role of the CeO_2 intermediate layer, was constructed and is shown in Fig. 1.

A critical processing requirement is to prevent partial reduction of CeO_2 to Ce_2O_3, which is not lattice-matched to CZTS and exhibits less favorable optoelectronic properties. Ce_2O_3 crystallizes in a hexagonal

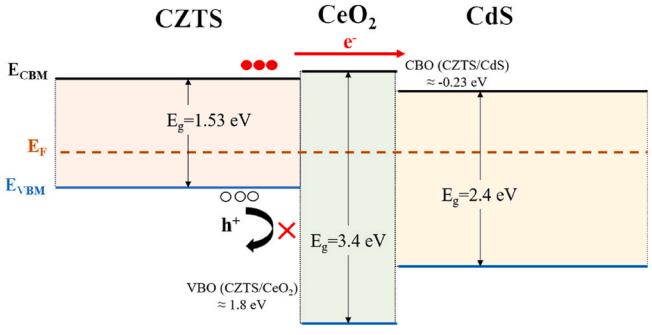

Fig. 1. Schematic representation of the proposed energy band alignment of the CZTS/CeO_2/CdS heterojunction, illustrating the hole-blocking effect of the CeO_2 intermediate layer.

structure (space group *P3m*1) with lattice constants $a = b = 3.89$ Å and $c = 6.18$ Å, and has a narrower bandgap of approximately ~2.4 eV compared with CeO_2 [26,30,31]. The formation of Ce_2O_3 could therefore increase parasitic absorption and introduce additional structural and electronic mismatch at the interface, counteracting the intended recombination suppression.

In the present work, the preparation of CeO_2 interlayers was systematically investigated and optimized using two different methods: chemical bath deposition (CBD) and pulsed laser deposition (PLD). The influence of the optimized CeO_2 interlayer on the performance of CZTS MGL and thin film solar cells is evaluated.

2. Experimental

2.1. Preparation of CeO_2 by chemical bath deposition

CeO_2 films were deposited by chemical bath deposition on soda-lime glass (SLG), SiO_2 and CZTS monograin powder crystals at 60 °C in a weakly acidic solution (pH~6) containing 0.01M $Ce(CH_3COO)_3$ and 0.005M $KClO_3$ in deionized water under continuous stirring. The deposition time was varied from 10 to 60 min. In selected experiments, the deposition was repeated over multiple consecutive cycles under identical conditions to increase the layer thickness. This approach was used to assess the capability of the CBD method for controlled thickness variation. The chemical reactions expected to occur during the process include the oxidation of Ce^{3+} to Ce^{4+} (Eq. (1)), followed by spontaneous hydrolysis of Ce^{4+} leading to CeO_2 formation (Eq. (2)) [32].

$$2Ce^{3+} + ClO_3^- \rightarrow 2Ce^{4+} + ClO_2^- \quad (1)$$

$$Ce^{4+} + 2H_2O \rightarrow CeO_2 + 4H^+ \quad (2)$$

2.2. Preparation of CeO_2 by pulsed laser deposition

CeO_2 films were deposited by pulsed laser deposition on SLG, SiO_2, CZTS MGL membranes and thin films at room temperature. A Neocera Pioneer 120 PLD system equipped with a UV excimer laser ($\lambda = 248$ nm, Coherent Compex Pro 102 F) was used. The laser beam was focused onto an area of approximately 5 mm^2 on the CeO_2 target, with a target-to-substrate distance of 9 cm. During deposition, the substrate was rotated to ensure uniform distribution of the ablated material, while the target was rastered to achieve uniform consumption of its surface and avoid local overheating. Depositions were performed under two different ambient conditions: in an oxygen background pressure of 50 mTorr and under high dynamic vacuum around 10^{-5} Torr. The number of laser pulses was varied from 20 to 3000, while all other deposition parameters were kept constant (pulse repetition rate: 3 Hz; pulse energy: 200 mJ).

2.3. Fabrication of CZTS monograin layer and thin film devices

The schematic structure of MGL solar cell, consisting of Au/CZTS/CeO_2/CdS/*i*-ZnO/ZnO:Al/Ag/glass is shown in Fig. 2a. The CZTS absorber, in the form of monograin powder, was synthesized from high purity (99.999%) binary precursors in a KI (99.99%) molten salt medium sealed in evacuated quartz ampoules [33]. The growth mechanisms of CZTS monograin powders in a molten salt medium have been extensively described in previous studies [34–39]. Before implementing the monograins as absorber layer in MGL solar cells, the powder crystals underwent sequence of post-treatments. The powder crystal surfaces were first cleaned and chemically etched for 5 min in a 1% v/v Br_2–MeOH solution, followed by etching for 5 min in a 10% m/m KCN solution. The etched monograins were subsequently post-annealed in a dual-zone tube furnace at 840 °C in sulfur atmosphere ($P_S = 2050$ Torr) for 60 min.

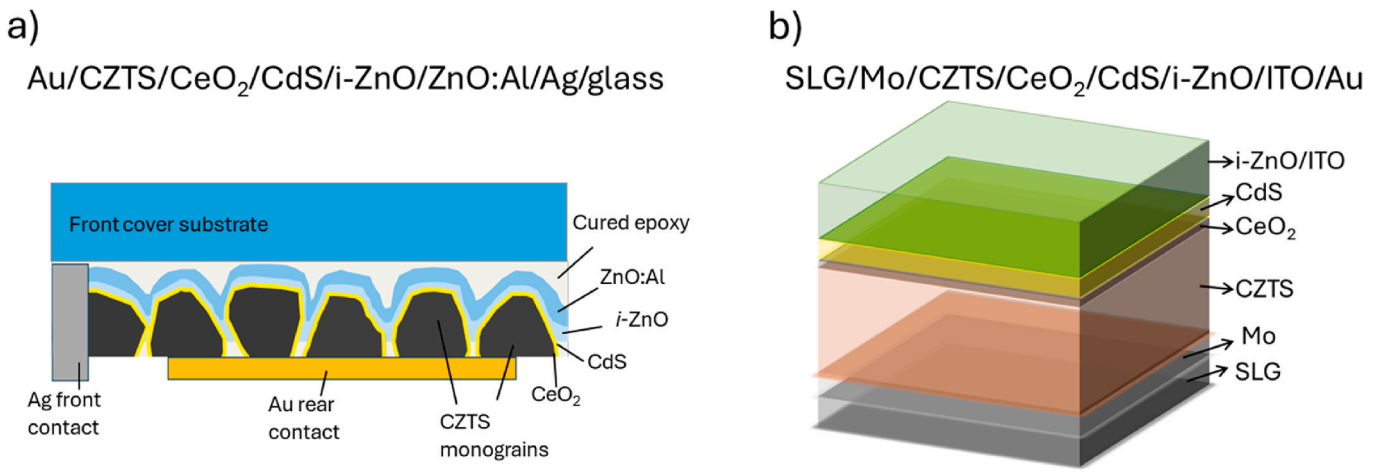

Fig. 2. Schematic structure of CZTS solar cells: a) monograin layer; and b) thin film configuration.

The post-treated CZTS powder crystals were then partially embedded in an epoxy layer coated onto a transparent substrate to form the so-called monograin membrane. After complete polymerization, the membrane surface was covered with CeO_2 by PLD process. A CdS buffer layer was subsequently deposited onto the CeO_2 covered monograin membrane from alkaline solution by the CBD method [40]. This was followed by deposition of an *i*-ZnO/ZnO:Al window layer by radio-frequency (RF) magnetron sputtering process. Finally, Ag-paste was applied as front collector, and the structure was sealed onto a glass substrate using a transparent polymer adhesive. A more detailed description of the MGL device preparation can be found in Ref. [33] [41].

The schematic structure of the CZTS thin-film solar cell (SLG/Mo/CZTS/CeO_2/CdS/i-ZnO/ITO/Au) is illustrated in Fig. 2b. CZTS thin films were deposited on Mo-coated SLG substrates by a spin-coating technique. The CZTS precursor solution was prepared by dissolving 40.7 mmol of thiourea (TU), 9.35 mmol of CuCl, 5 mmol of $SnCl_2{\cdot}2H_2O$, and 6 mmol of $ZnCl_2$ in 10 mL of dimethylformamide (DMF). The solution was heated to 80 °C until complete dissolution was achieved. The resulting CZTS solution was spin-coated onto cleaned Mo-coated SLG substrates at 3000 rpm for 30 s, followed by a short annealing step at 350 °C for 2 min and a cooling period of 5 min. This coating and annealing cycle was repeated 10 times to obtain a CZTS absorber layer with a thickness of approximately 1.5 μm. The absorber layer deposition was performed entirely under ambient air conditions. Subsequently, sulfurization was carried out in an OTF-1200X tube furnace using 0.3 g of sulfur placed in a graphite box. The temperature was ramped up at a rate of 20 °C min^{-1} to 650 °C and maintained at this temperature for 20 min under an Ar atmosphere. After sulfurization, CeO_2 layers of varying thicknesses were deposited by PLD. Subsequently, a CdS buffer layer (~50 nm) was deposited by CBD, followed by deposition of ~50 nm of i-ZnO and 250 nm of ITO using RF magnetron sputtering. Finally, Au top contact grids (d~100 nm) were deposited through a shadow mask using a sputtering system. The device area was defined by mechanical scribing, resulting in an active area of approximately 0.22 cm^2. Additional details of the fabrication process are provided in our previous work [42].

2.4. Characterization

The morphology of the Ce-O layers deposited on the surfaces of CZTS powder crystals was investigated using a Zeiss Ultra 55 high-resolution scanning electron microscope (SEM). Imaging was performed in in-lens secondary electron mode at an accelerating voltage of 4 kV. The chemical states of the Ce–O layers were studied by X-ray photoelectron spectroscopy (XPS) using a Kratos Analytical Axis Ultra DLD spectrometer operated under ultrahigh vacuum conditions (base pressure 10^{-9} mbar). The instrument was equipped with a monochromatic Al Kα X-ray source and an achromatic Mg Kα/Al Kα dual-anode X-ray source. The achromatic Mg Kα source was used to collect secondary survey spectra to distinguish and separate the core-level and Auger peaks in the XPS spectra. The optical transmittance of the CeO_2 layers deposited on SLG substrates was measured using a Shimadzu UV-1800 Ultraviolet–Visible-Near-Infrared (UV–Vis–NIR) spectrophotometer in the wavelength range of 300-1000 nm.

The electrical performance of CZTS monograin layer and thin film solar cells was characterized by current-voltage (J-V) measurements using a Keithley 2400 source meter under standard test conditions (AM 1.5, 100 mW/cm^2) using a Newport Oriel Class A 91195A solar simulator. Considering that the active working area of the MGL solar cells is around 75% of the total area [43], the power conversion efficiency values were re-calculated for the active area (η_{active}).

3. Results and discussion

The morphology of the CeO_2 films was analysed by SEM, and representative images are presented in Figs. 3 and 4. For CBD, a uniform and continuous CeO_2 layer with good surface coverage was obtained on CZTS MGP crystals. However, the experimental results indicated that the Ce-O layer thickness remained nearly constant under the applied deposition conditions, showing no dependence on the deposition time. Cross-sectional SEM images of CeO_2 films deposited on CZTS MGP crystals by CBD at 60 °C for 10 min, three consecutive 10-min cycles, and 60 min are shown in Fig. 3a–c.

For PLD, deposition under an oxygen background pressure resulted in a uniformly distributed CeO_2 layer with a structurally porous morphology (Fig. 4a). In contrast, deposition under high vacuum conditions (Fig. 4b) yielded a uniform, smooth layer with good surface coverage. These results demonstrate that the morphology of the CeO_2 layer can be controlled by adjusting the PLD deposition environment. A cross-sectional SEM image of a CZTS MGP crystal coated with a CeO_2 layer deposited by PLD in vacuum, followed by CdS deposition via CBD, is shown in Fig. 4c. The image confirms that the CeO_2 layer remains stable during the subsequent CBD process and is not dissolved in the CdS deposition solution.

UV-Vis measurements were performed on CeO_2 deposited on SLG substrates by CBD and PLD. The optical bandgap energies were determined from transmittance data using Tauc plots. As shown in Fig. 5, the band gap of the CeO_2 films was 3.46 eV for CBD and 3.38 eV for PLD, these values correlate well with the literature [25,26].

The valence state of Ce in the samples was determined by XPS measurements. For Ce-O films deposited on SiO_2 by either PLD or CBD,

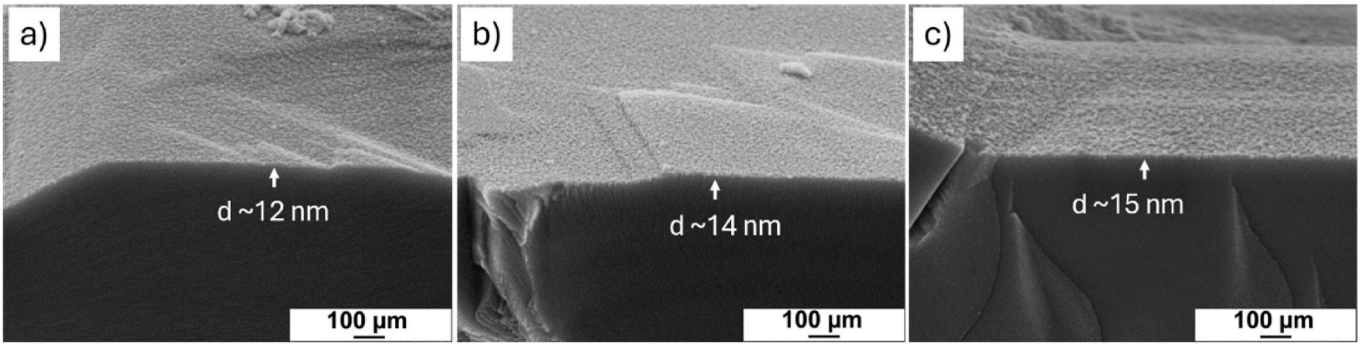

Fig. 3. The cross-sectional SEM images of a CeO_2 films deposited on CZTS MGP crystals by CBD at 60 °C: a) 10 min; b) 3 × 10 min; and c) 60 min.

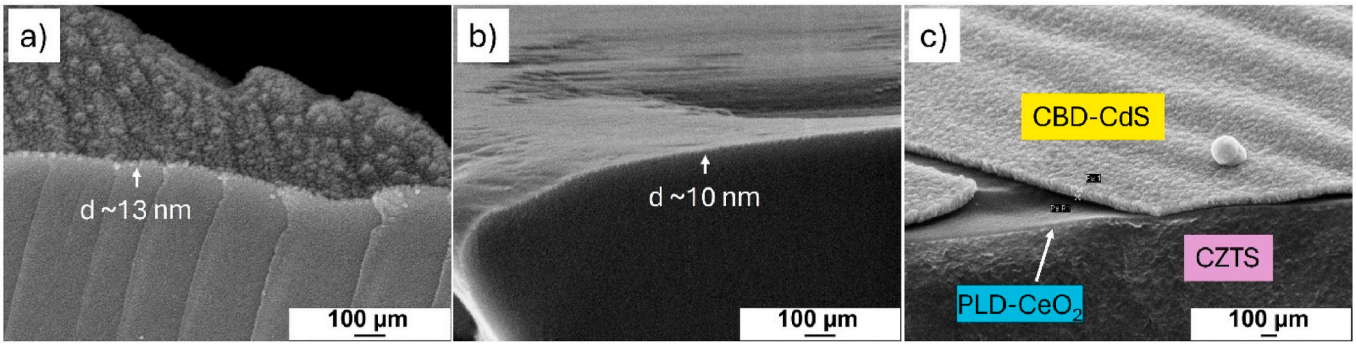

Fig. 4. The cross-sectional SEM images of CeO_2 films deposited on CZTS MGP crystals by PLD: a) under an oxygen backgroundpressure; b) under high vacuum; and c) CZTS coated with PLD-CeO_2 deposited under high vacuum, followed by CBD-CdS.

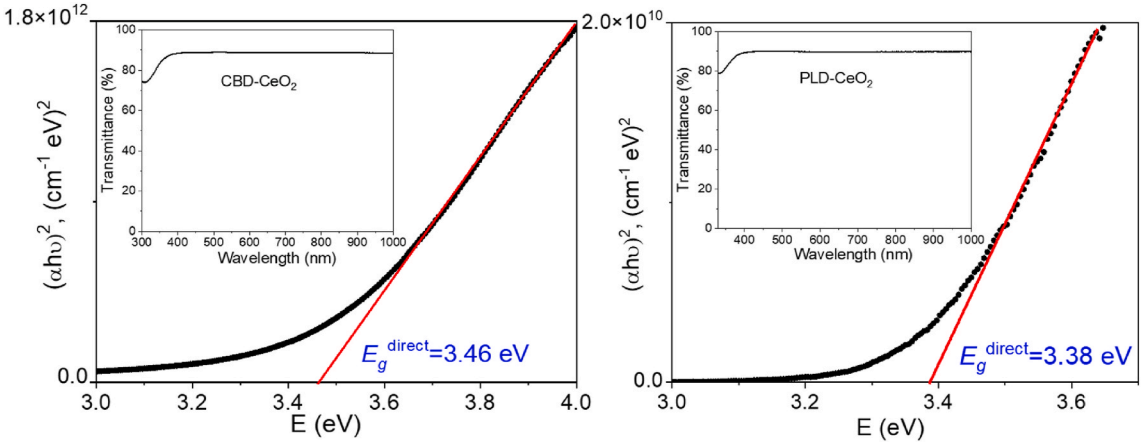

Fig. 5. Direct Tauc plots used for band gap determination of CeO_2 thin films deposited on soda-lime glass by CBD (left) and PLD (right). UV-Vis transmittance spectra are shown in the inset graphs.

the Ce 3d core level spectra (Fig. 6a) are dominated by the characteristic Ce^{4+} multiplet (shown in green) associated with CeO_2 [33]. The peaks labelled as u, u_2 and u_3 correspond to the Ce^{4+} $3d_{3/2}$ chemical states, while v, v_2 and v_3 correspond to the Ce^{4+} $3d_{5/2}$ states. Their fitted binding energies are located at about 900.5 eV (u), 906.9 eV (u_2), and 916.3 eV (u_3) for the $3d_{3/2}$ components, and 882.0 eV (v), 888.2 eV (v_2), and 897.9 eV (v_3) for the $3d_{5/2}$ components. In addition, weaker features assigned to Ce^{3+} (shown in yellow) are observed at 896.1 eV (u_0) and 902.9 eV (u_1) for the $3d_{3/2}$ states, and at 880.5 eV (v_0) and 884.2 eV (v_1) for the $3d_{5/2}$ states [33].

These results indicate that both PLD- and CBD-grown films on SiO_2 are predominantly composed of CeO_2, with a minor contribution from Ce^{3+} species. It should be noted that the presence of Ce^{3+} does not definitely confirm the formation of Ce_2O_3 during deposition, as partial reduction of CeO_2 may also occur during prolonged X-ray exposure or ion beam sputtering [44,45]. In this context, the intense peak at approximately 916-917 eV is particularly important, as it is a characteristic peak distinguishing Ce^{4+} from Ce^{3+} [45–47].

A significantly different behaviour was observed for Ce-O films deposited on CZTS powder by the CBD method (see Fig. 6b). The spectrum exhibits only Ce^{3+} related features, with peaks at 900.2 eV (u_0) and 903.8 eV (u_1) assigned to Ce^{3+} $3d_{3/2}$ states, and peaks at 882.1 eV (v_0) and 885.7 eV (v_1) assigned to Ce^{3+} $3d_{5/2}$ states. Notably, the Ce^{4+} components characteristic of CeO_2, including the feature near 916 eV, are absent, indicating the formation of the undesired Ce_2O_3 phase. For comparison, Ce-O films deposited by CBD on SiO_2 substrate in the same

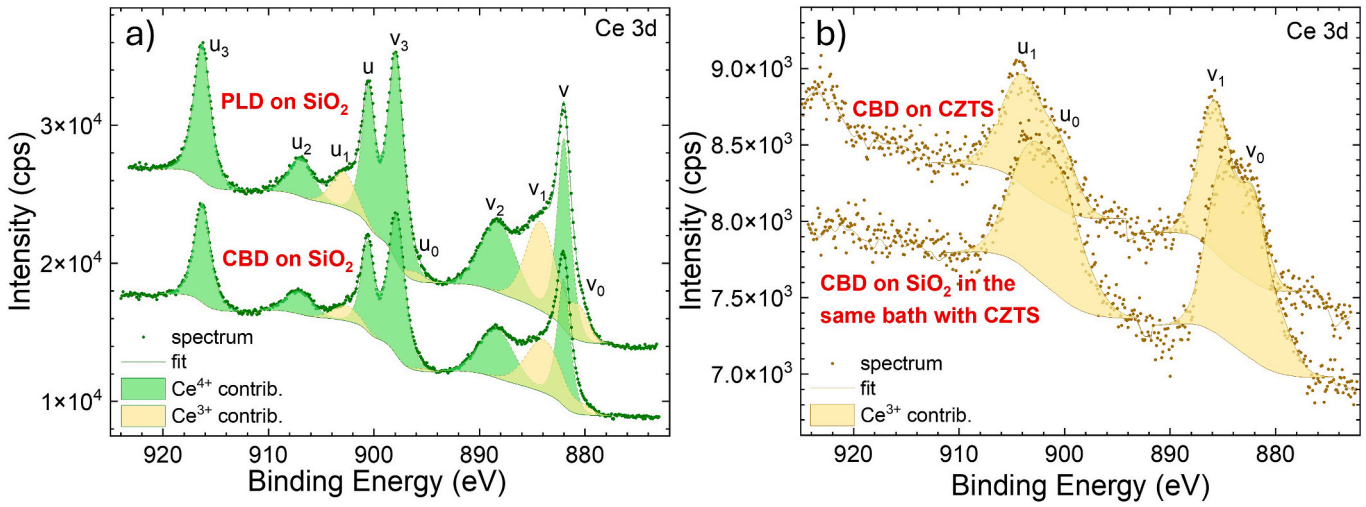

Fig. 6. Ce 3d XPS spectra of Ce-O films a) deposited on SiO_2 by PLD and CBD; and b) deposited by CBD on CZTS and on SiO_2 in the same bath with CZTS. Peaks labelled as u, u_2 and u_3 refer to Ce^{4+} $3d_{3/2}$ states, while v, v_2 and v_3 refer to Ce^{4+} $3d_{5/2}$ states. The characteristic peaks of Ce^{3+} $3d_{3/2}$ and $3d_{5/2}$ states are labelled as u_0, u_1 and v_0, v_1, respectively.

bath together with CZTS powder exhibited identical behaviour. These results suggest that CBD on CZTS powder predominantly leads to the formation of Ce_2O_3, and that the presence of CZTS powder in the solution also promotes Ce_2O_3 formation on SiO_2. This behaviour is likely associated with partial dissolution or surface modification of CZTS crystal in the deposition solution, which alters the local redox environment. The presence of dissolved species (e.g., Cu^+/Cu^{2+}, Sn^{2+}/Sn^{4+}, or sulfide-related species) may shift the oxidation–reduction balance, inhibiting complete oxidation of Ce^{3+} to Ce^{4+} and favoring the formation of Ce_2O_3. This indicates that the substrate plays an active role in determining the phase formation during CBD, highlighting a key limitation of solution-based deposition for this system.

Therefore, to evaluate the influence of the intermediate layer and its thickness on CZTS MGL device performance, CeO_2 films were deposited by PLD. As a first step, the effect of the deposition atmosphere was examined by comparing solar cells with CeO_2 layers prepared under high vacuum and in an O_2 background pressure. As shown in Fig. 7, the deposition environment strongly affects the photovoltaic response of the cells. Under otherwise identical conditions (100 laser pulses), the device

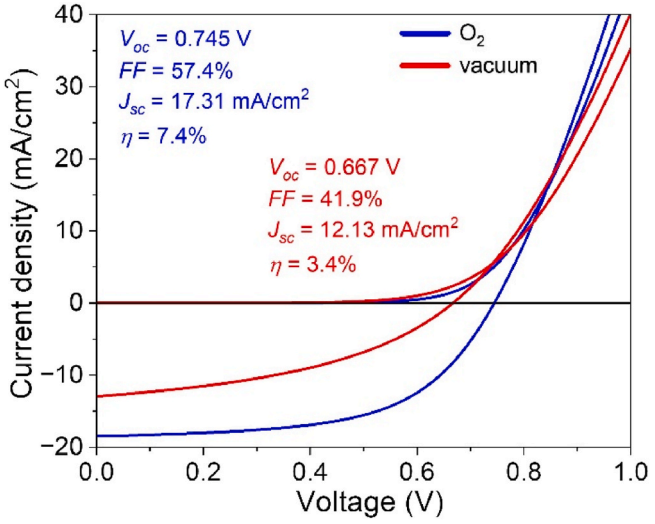

Fig. 7. The *J-V* characteristics of CZTS MGL solar cells with CeO_2 intermediate layer deposited by PLD under an oxygen background pressure and under high vacuum.

with CeO_2 deposited under O_2 background pressure exhibited markedly better performance, with $V_{oc} = 0.745$ V, $J_{sc} = 17.31$ mA/cm^2, $FF = 57.4\%$, and $\eta = 7.4\%$, whereas the cell with CeO_2 deposited under vacuum reached only $V_{oc} = 0.667$ V, $J_{sc} = 12.13$ mA/cm^2, $FF = 41.9\%$, and $\eta = 3.4\%$. The less pronounced diode-like behavior of the vacuum-deposited sample indicates deterioration of the junction quality and increased carrier transport losses. Overall, these initial results demonstrated that, under the applied conditions, an oxygen atmosphere is more suitable for CeO_2 deposition than high dynamic vacuum.

Consequently, CeO_2 films were deposited on CZTS MGP crystals under oxygen background pressure of 50 mTorr with the number of laser pulses varied from 20 to 3000 to control the film thickness.

SEM analysis revealed a strong dependence of the CeO_2 film thickness on the number of laser pulses, ranging from ~41 nm for 3000 pulses to ~5 nm for 100 pulses (see Fig. 8). At lower pulse counts, the deposited films became too thin to be reliably measured by SEM, indicating that the deposition rate decreases proportionally with the reduction in pulse count.

The characteristic *J–V* parameters of MGL solar cells as a function of CeO_2 layer thickness on CZTS monograins are presented in Fig. 9. The data are based on measurements of 10 solar cells with a contact area of 4.5 mm^2. The performance of MGL solar cells shows a strong dependence on CeO_2 thickness. The open-circuit voltage (V_{oc}) remained relatively stable (760-780 mV) up to 100 pulses, after which it gradually decreases. This trend suggests that thicker CeO_2 films deposited at higher pulse counts may introduce resistive barriers at the interface. The fill factor (*FF*) exhibits a similar trend, maintaining values above 60% at low pulse counts but decreasing sharply beyond 75 pulses, indicating increased series resistance or limitations in charge transport. The short-circuit current density (J_{sc}) initially increased, reaching a maximum at around 100 pulses, and then decreased at higher pulse counts. This behaviour indicates the existence of an optimal thickness range in which the CeO_2 layer effectively functions as a hole-blocking layer, while a thicker layer hinders charge collection.

Consequently, the overall power conversion efficiency follows a similar trend, reaching a maximum of 9.0% at the optimal CeO_2 thickness (~75 pulses), and decreasing at higher thicknesses due to the reductions in *FF*, V_{oc} and J_{sc}. At lower pulse counts (20-50 pulses), the CeO_2 layer is likely discontinuous; although the device parameters are improved compared to the reference sample (without CeO_2 layer), they remain lower than those achieved with an optimal CeO_2 thickness.

These trends are directly reflected in the shape of the illuminated *J-V* curves (Fig. 10). The reference device without CeO_2 exhibits a typical

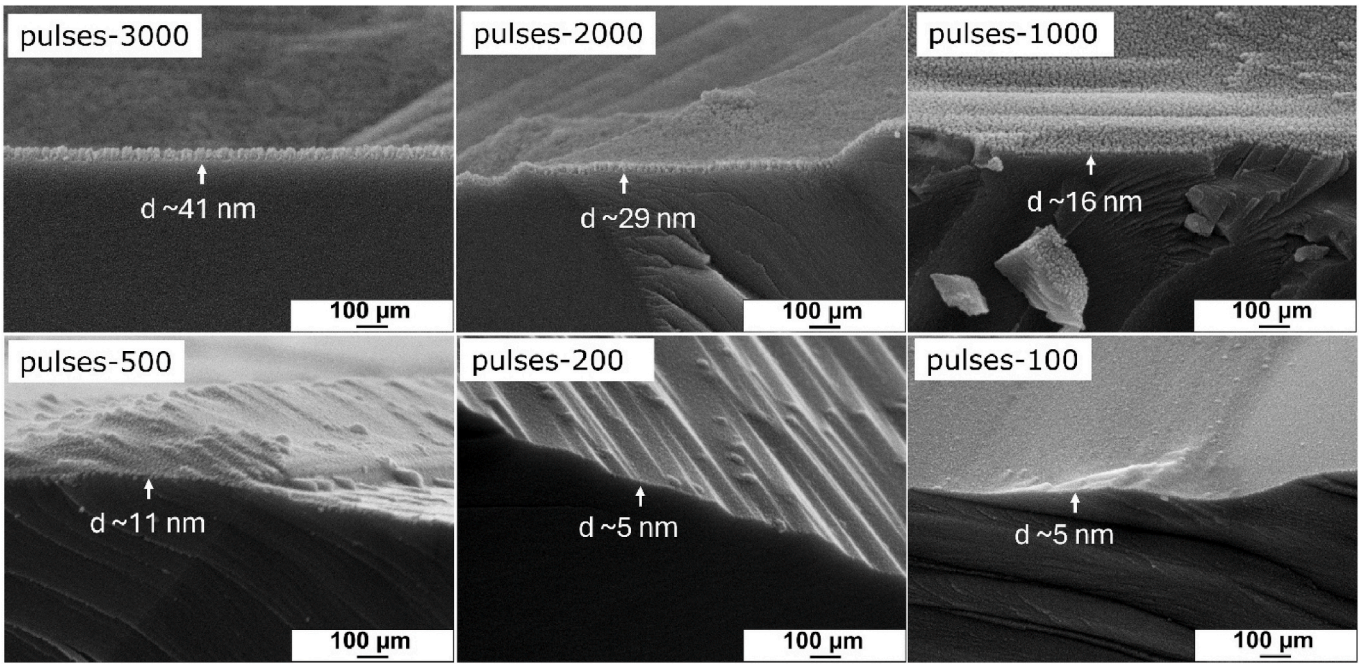

Fig. 8. Cross-sectional SEM images of CeO_2 layers deposited on CZTS MGPs by PLD with different laser pulse numbers, demonstrating the decrease in layer thickness with reduced pulse counts.

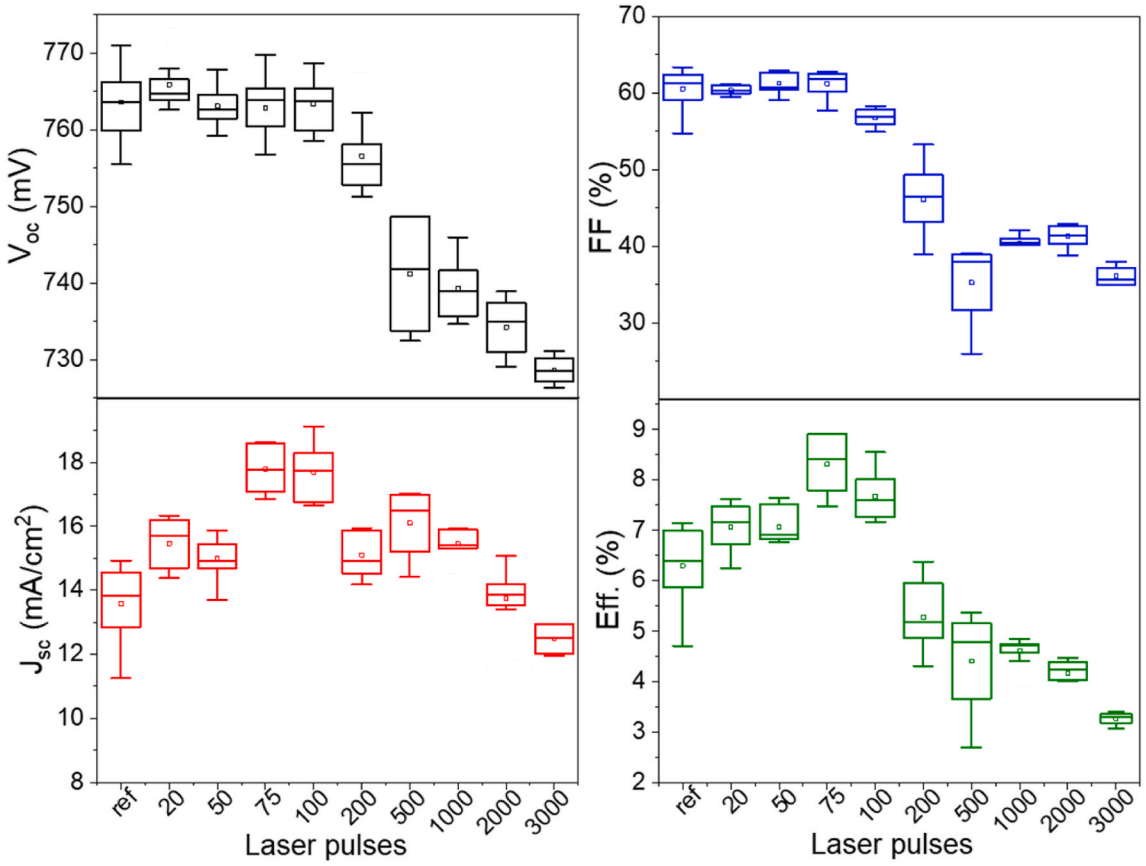

Fig. 9. Box plots of open-circuit voltage (V_{oc}), short-circuit current density (J_{sc}), fill factor (*FF*) and efficiency (*Eff.*) of CZTS MGL solar cells as a function of CeO_2 layer thickness, which was controlled by varying the number of PLD laser pulses from 20 to 3000.

diode-like photovoltaic response. After deposition of CeO_2 (75 pulses), the *J-V* characteristics show an increase in J_{sc} together with enhanced forward current at a given applied voltage, indicating improved charge collection. In contrast, the device with a thicker CeO_2 layer (3000 pulses) exhibits an S-shaped or double-diode-like response in the forward-bias region. This S-shaped *J–V* behavior is characteristic of transport-

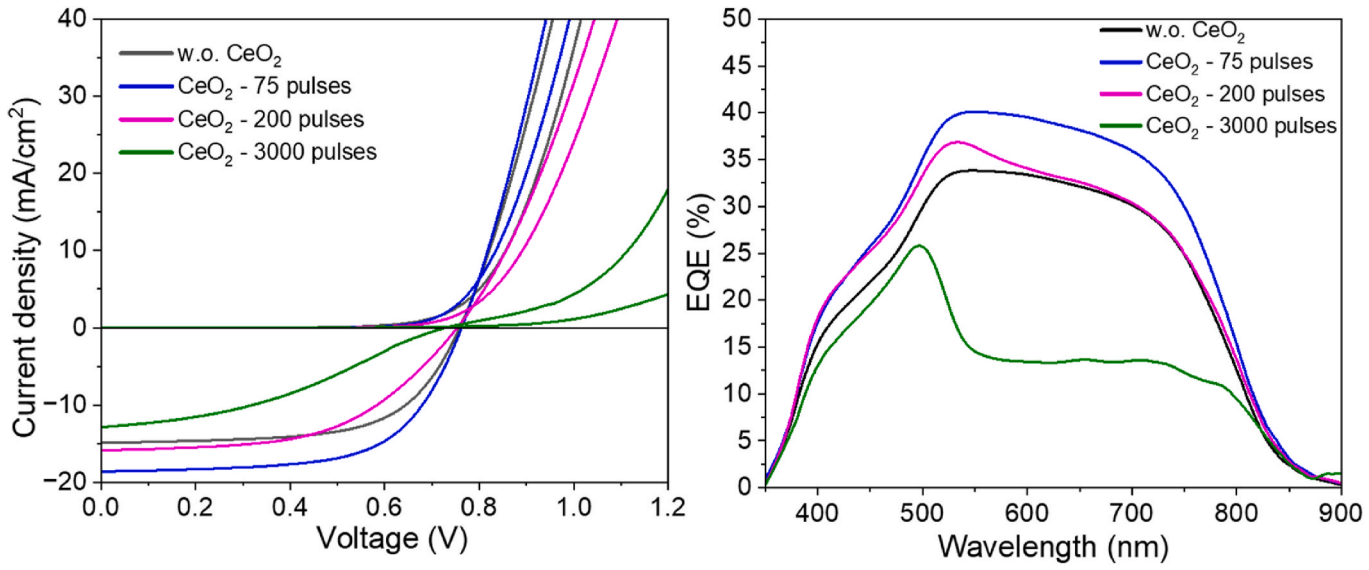

Fig. 10. *J-V* characteristics (left) and EQE spectra (right) of CZTS MGL solar cells without and with CeO_2 layer deposited by PLD using 75, 200 and 3000 laser pulses, representing optimal and excessively thick layers, respectively.

limited interfaces and can be attributed to the formation of an energy barrier that prevents carrier extraction. In this case, the increased thickness of CeO_2 layer reduces tunneling probability and enhances carrier accumulation at the interface, leading to recombination and pronounced reduction in *FF*. This behaviour is consistent with previous reports on intermediate layers acting as overly thick insulating barriers [48,49].

The EQE spectra (Fig. 10) are in good agreement with the *J-V* characteristics. Compared to the reference device, the solar cell with the optimally thin CeO_2 layer (75 pulses) exhibits an almost spectrally uniform increase in EQE over the 450-820 nm wavelength range, corresponding to the observed increase in J_{sc}. The spectrally uniform increase suggests improved photocarrier collection rather than wavelength-selective optical enhancement. This behavior is consistent with reduced interfacial carrier losses at the CdS/CZTS heterojunction due to the hole-blocking and/or passivating effect of the ultrathin CeO_2

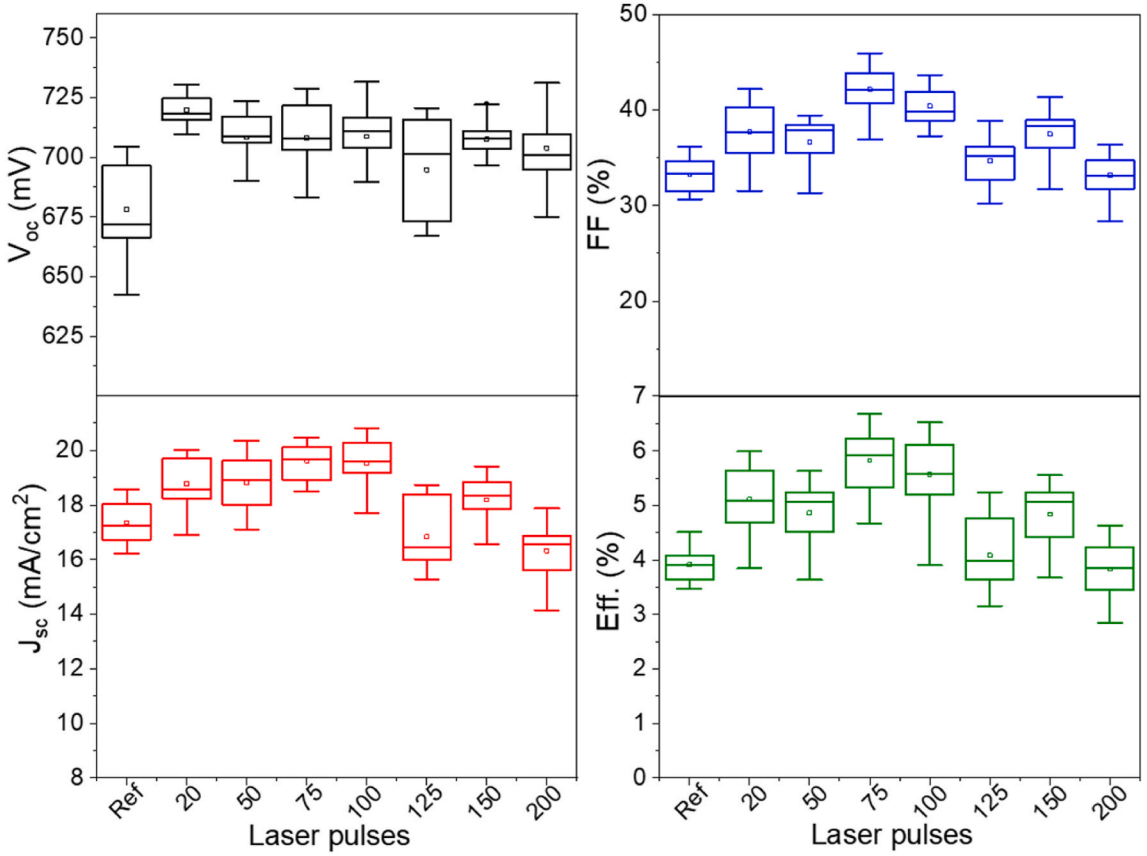

Fig. 11. Box plots of open-circuit voltage (V_{oc}), short-circuit current density (J_{sc}), fill factor (*FF*) and efficiency (*Eff.*) of CZTS thin film solar cells as a function of CeO_2 layer thickness, which was controlled by varying the number of PLD laser pulses from 20 to 200.

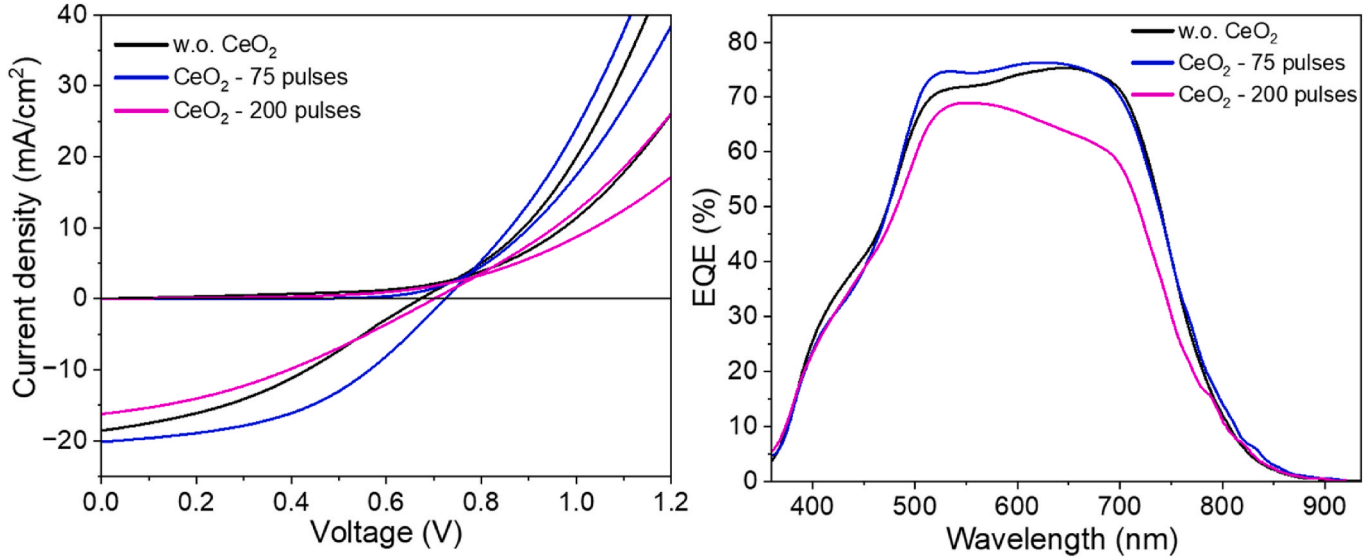

Fig. 12. *J-V* characteristics (left) and EQE spectra (right) of the CZTS thin film solar cells without and with CeO_2 layer deposited by PLD using 75 and 200 laser pulses.

layer. In comparison, solar cells with thicker CeO_2 layers (200 and 3000 pulses) exhibit progressive reduction in EQE, with a pronounced decrease in the 500-800 nm range for the sample prepared with 3000 pulses. The observed decrease in EQE is consistent with the corresponding reduction in J_{sc} and the transport-limited *J-V* characteristics, confirming the strong dependence of device performance on the CeO_2 thickness.

The effect of the CeO_2 intermediate layer was also investigated in CZTS thin-film solar cells. Based on the MGL solar cell results, where CeO_2 depositions above 100 laser pulses led to performance deterioration, a relatively low deposition range was selected for thin-film devices to investigate the effect of increasing CeO_2 thickness and to assess the onset of possible detrimental effects at higher thicknesses. CeO_2 layers were deposited on CZTS thin films in an oxygen background of 50 mTorr, with the number of laser pulses varied from 20 to 200. The corresponding photovoltaic parameters as a function of CeO_2 layer thickness are presented in Fig. 11. The data are based on measurements of 16 solar cells with a contact area of 22 mm^2.

For CZTS thin film solar cells, all device parameters showed improvement compared to the reference cell without CeO_2 intermediate layer, resulting in an increase in device efficiency from 4.5% to 6.7%. This enhancement is mainly attributed to a significant increase in *FF* from 36% to 46% and an improvement in V_{oc} from 703 mV to 731 mV. Similar to the MGL solar cells, the highest efficiency for the CZTS thin film devices was obtained for CeO_2 layer deposited using 75 pulses.

The *J-V* characteristics and EQE spectra of the thin-film solar cells (see Fig. 12) follow the same overall trend as observed for the MGL devices. The solar cell with the optimally thin CeO_2 layer (75 pulses) shows the highest EQE over most of the measured spectral range, whereas solar cells with thicker CeO_2 layer (200 pulses) exhibits a lower EQE response. This trend is consistent with the *J-V* characteristics and indicates that the variation in J_{sc} is mainly related to differences in charge carrier collection.

These results demonstrate that a carefully optimized CeO_2 intermediate layer can significantly enhance the performance of CZTS solar cells, independent of device architecture. However, excessive layer thickness introduces optical and electrical losses that ultimately degrade device efficiency. Given the strong dependence of photovoltaic parameters on CeO_2 thickness, further optimization is required, particularly to achieve precise thickness control and to improve the structural and electronic quality of the CeO_2 layer.

4. Conclusions

This study demonstrates that the introduction of ultrathin CeO_2 intermediate layer at the heterointerface between the *p*-type CZTS absorber and the *n*-type CdS buffer effectively enhances carrier collection. While both CBD and PLD produced uniform Ce-O layers with good surface coverage on CZTS monograin powder crystals; XPS analysis revealed that CBD predominantly resulted in Ce_2O_3 formation, whereas PLD enabled the deposition of stoichiometric CeO_2 with controlled thickness. SEM analysis showed that the thickness of PLD-CeO_2 films increased from ~5 nm (100 pulses) to ~41 nm (3000 pulses), exhibiting non-linear dependence on pulse number. Ultrathin CeO_2 layers (<5 nm), achieved at 75–100 pulses, were found to be optimal, effectively acting as hole-blocking layers without introducing significant transport barriers. Incorporation of these optimized CeO_2 interlayers into both monograin layer and thin-film CZTS solar cells led to substantial performance improvements, with power conversion efficiency increasing from 7.1% to 9.0% and from 4.5% to 6.7%, respectively. Despite the observed improvements, the overall device efficiency remains below the current state-of-the-art for CZTS-based solar cells. This indicates that bulk and interface defects in addition to other loss mechanisms still limit device performance. Therefore, the CeO_2 interlayer should be considered as part of a broader interface and absorber optimization strategy.

CRediT authorship contribution statement

K. Timmo: Conceptualization, Data curation, Formal analysis, Investigation, Methodology, Project administration, Validation, Visualization, Writing – original draft. **M. Pilvet:** Methodology. **M. Danilson:** Formal analysis, Investigation. **V. Mikli:** Formal analysis, Investigation. **J. Krustok:** Formal analysis, Investigation, Writing – review & editing. **A. Dolski:** Methodology. **A. Nasyori:** Methodology. **S. Bereznev:** Methodology. **M. Grossberg-Kuusk:** Funding acquisition, Writing – review & editing. **M. Kauk-Kuusik:** Formal analysis, Funding acquisition, Writing – review & editing.

Declaration of competing interests

The authors declare that they have no known competing financial interests or personal relationships that could have appeared to influence the work reported in this paper.

Acknowledgments

This work was supported by the European Union through the European Regional Development Fund, Project TK210U7, by the Estonian Research Council grant PRG1023 and the research was conducted using the NAMUR + core facility funded by the Estonian Research Council (TTK26).

Data availability

Data will be made available on request.

References

[1] S. Giraldo, Z. Jehl, M. Placidi, V. Izquierdo-Roca, A. Pérez-Rodríguez, E. Saucedo, Progress and perspectives of thin film kesterite Photovoltaic technology: a critical review, Adv. Mater. 31 (2019) 1806692, https://doi.org/10.1002/adma.201806692.

[2] A. Wang, M. He, M.A. Green, K. Sun, X. Hao, A critical review on the progress of kesterite solar cells: current strategies and insights, Adv. Energy Mater. 13 (2023) 2203046, https://doi.org/10.1002/aenm.202203046.

[3] C. Cui, Y. Li, H. Wei, X. Du, Z. Shao, D. Kou, Z. Wu, S. Xia, X. Feng, S. Pang, X. Wang, S. Mao, H. Xin, S. Wu, G. Cui, Regulating grain growth via Li_2SnS_3 interphase in kesterite solar cells with certified efficiencies exceeding 15%, Nat. Energy (2026) https://doi.org/10.1038/s41560-026-01987-x.

[4] P. Luo, S. Chen, G. Chen, M. Abbas, Z. Su, Z. Zheng, H. Ma, X. Zhang, G. Liang, Quasi-epitaxial heterojunction interface reconstruction enables 11.96% certified efficiency in Cd-free Cu_2ZnSnS_4 solar cells, Sci. Adv. 12 (2026) eaee0270, https://doi.org/10.1126/sciadv.aee0270.

[5] M. He, K. Sun, M.P. Suryawanshi, J. Li, X. Hao, Interface engineering of p-n heterojunction for kesterite photovoltaics: a progress review, J. Energy Chem. 60 (2021) 1–8, https://doi.org/10.1016/j.jechem.2020.12.019.

[6] N. Singh, Sonika, sustainability-driven advances in kesterite solar cells: strategies, challenges, future directions, Appl. Mater. Today 45 (2025) 102840, https://doi.org/10.1016/j.apmt.2025.102840.

[7] T. Liu, L. Han, L. Pei, X. Zhong, W. Yang, K. Leng, Q. Zeng, D. Kou, Z. Zhou, F. Liu, S. Wu, Efficient CZTSSe solar cells with the highest V_{OC} of 591 mV enabled by thermal sputtering ITO, Sci. China Mater. 69 (2026) 1677–1690, https://doi.org/10.1007/s40843-025-3773-7.

[8] T. Wu, S. Chen, Z. Su, Z. Wang, P. Luo, Z. Zheng, J. Luo, H. Ma, X. Zhang, G. Liang, Heat treatment in an oxygen-rich environment to suppress deep-level traps in Cu_2ZnSnS_4 solar cell with 11.51% certified efficiency, Nat. Energy 10 (2025) 630–640, https://doi.org/10.1038/s41560-025-01756-2.

[9] J. Krustok, K. Timmo, M. Kauk-Kuusik, M. Grossberg-Kuusk, Tunneling-enhanced interface recombination and current loss curves in kesterite solar cells, Appl. Phys. Lett. 123 (2023) 242102, https://doi.org/10.1063/5.0175082.

[10] D. Schmid, M. Ruckh, F. Grunwald, H.W. Schock, Chalcopyrite/defect chalcopyrite heterojunctions on the basis of $CuInSe_2$, J. Appl. Phys. 73 (1993) 2902–2909, https://doi.org/10.1063/1.353020.

[11] O. Cojocaru-Mirédin, D. Hariskos, W. Hempel, A. Kanevce, X. Jin, J. Keutgen, M. Raghuwanshi, R. Schneider, R. Scheer, D. Gerthsen, W. Witte, Ordered vacancy compound Formation at the interface of $Cu(In,Ga)Se_2$ Absorber with Sputtered In_2S_3-Based buffers: an atomic-scale perspective, Sol. RRL 8 (2024) 2400574, https://doi.org/10.1002/solr.202400574.

[12] Y. Zhao, S. Yuan, Q. Chang, Z. Zhou, D. Kou, W. Zhou, Y. Qi, S. Wu, Controllable formation of ordered vacancy compound for high efficiency solution processed $Cu(In,Ga)Se_2$ solar cells, Adv. Funct. Mater. 31 (2021) 2007928, https://doi.org/10.1002/adfm.202007928.

[13] Y. Li, H. Wei, C. Cui, X. Wang, Z. Shao, S. Pang, G. Cui, CZTSSe solar cells: insights into interface engineering, J. Mater. Chem. A Mater 11 (2023) 4836–4849, https://doi.org/10.1039/D2TA09561K.

[14] Y.S. Ocak, F. Bayansal, Advancing earth-abundant CZTSSe solar cells: recent progress in efficiency and defect engineering, Nanomaterials 15 (2025), https://doi.org/10.3390/nano15211617.

[15] X. Yuan, J. Huang, J. Li, K. Sun, A. Wang, X. Hao, Device postannealing with superficially Ag-Modified absorber for high-efficiency Cd-Free Cu_2ZnSnS_4 solar cells, Small Sci. 6 (2026) e202500545, https://doi.org/10.1002/smsc.202500545.

[16] H. Sun, K. Sun, J. Huang, C. Yan, F. Liu, J. Park, A. Pu, J.A. Stride, M.A. Green, X. Hao, Efficiency enhancement of kesterite Cu_2ZnSnS_4 solar cells via solution-processed ultrathin tin oxide intermediate layer at absorber/buffer interface, ACS Appl. Energy Mater. 1 (2018) 154–160, https://doi.org/10.1021/acsaem.7b00044.

[17] W. Wu, Y. Cao, J. V Caspar, Q. Guo, L.K. Johnson, R.S. Mclean, I. Malajovich, K. R. Choudhury, Characterization of CZTSSe photovoltaic device with an atomic layer-deposited passivation layer, Appl. Phys. Lett. 105 (2014) 42108, https://doi.org/10.1063/1.4891852.

[18] M.E. Erkan, V. Chawla, M.A. Scarpulla, Reduced defect density at the CZTSSe/CdS interface by atomic layer deposition of Al_2O_3, J. Appl. Phys. 119 (2016) 194504, https://doi.org/10.1063/1.4948947.

[19] M.L. Kumar, J.L. Prasanna, A. Kumar, C. Santhosh, Tunneling layer for lowering recombination and efficiency enhancement in CZTS solar cell, Next Mater. 11 (2026) 101769, https://doi.org/10.1016/j.nxmate.2026.101769.

[20] Nisika, K. Kaur, K. Arora, A.H. Chowdhury, B. Bahrami, Q. Qiao, M. Kumar, Energy level alignment and nanoscale investigation of a-TiO_2/Cu-Zn-Sn-S interface for alternative electron transport layer in earth abundant Cu-Zn-Sn-S solar cells, J. Appl. Phys. 126 (2019) 193104, https://doi.org/10.1063/1.5121874.

[21] Y. Sun, D. Ding, Tailoring band alignment of $Cu_2ZnSn(S,Se)_4$/CdS interface by Al_2O_3 drives solar cell efficiency, J. Alloys Compd. 970 (2024) 172651, https://doi.org/10.1016/j.jallcom.2023.172651.

[22] E. Ojeda-Durán, K. Monfil-Leyva, J. Andrade-Arvizu, I. Becerril-Romero, Y. Sánchez, R. Fonoll-Rubio, M. Guc, Z.J. Li-Kao, J.A. Luna-López, E. Saucedo, High efficiency Cu_2ZnSnS_4 solar cells over FTO substrates and their CZTS/CdS interface passivation via thermal evaporation of Al_2O_3, J. Mater. Chem. C Mater. 9 (2021) 5356–5361, https://doi.org/10.1039/D1TC00880C.

[23] X. Cui, K. Sun, J. Huang, J.S. Yun, C.-Y. Lee, C. Yan, H. Sun, Y. Zhang, C. Xue, K. Eder, L. Yang, J.M. Cairney, J. Seidel, N.J. Ekins-Daukes, M. Green, B. Hoex, X. Hao, Cd-Free Cu_2ZnSnS_4 solar cell with an efficiency greater than 10% enabled by Al_2O_3 passivation layers, Energy Environ. Sci. 12 (2019) 2751–2764, https://doi.org/10.1039/C9EE01726G.

[24] Nisika, K. Kaur, M. Kumar, Progress and prospects of CZTSSe/CdS interface engineering to combat high open-circuit voltage deficit of kesterite photovoltaics: a critical review, J. Mater. Chem. A Mater 8 (2020) 21547–21584, https://doi.org/10.1039/D0TA06450E.

[25] S. Guo, H. Arwin, S.N. Jacobsen, K. Järrendahl, U. Helmersson, A spectroscopic ellipsometry study of cerium dioxide thin films grown on sapphire by rf magnetron sputtering, J. Appl. Phys. 77 (1995) 5369–5376, https://doi.org/10.1063/1.359225.

[26] M. Balestrieri, S. Colis, M. Gallart, G. Schmerber, M. Ziegler, P. Gilliot, A. Dinia, Photoluminescence properties of rare earth (Nd, Yb, Sm, pr)-doped CeO_2 pellets prepared by solid-state reaction, J. Mater. Chem. C 3 (2015) 7014–7021, https://doi.org/10.1039/C5TC00075K.

[27] S. Schorr, H.-J. Hoebler, M. Tovar, A neutron diffraction study of the stannite-kesterite solid solution series, Eur. J. Mineral 19 (2007) 65–73, https://doi.org/10.1127/0935-1221/2007/0019-0065.

[28] A. Crovetto, C. Yan, B. Iandolo, F. Zhou, J. Stride, J. Schou, X. Hao, O. Hansen, Lattice-matched Cu_2ZnSnS_4/CeO_2 solar cell with open circuit voltage boost, Appl. Phys. Lett. 109 (2016) 233904, https://doi.org/10.1063/1.4971779.

[29] X. Huo, H. Shen, X. Hu, Z. Hou, J. Saddique, Cu2ZnSnS4/CeO_2 heterojunction with excellent sensing property for ammonia nitrogen in aqueous solution, Semicond. Sci. Technol. 36 (2021) 95021, https://doi.org/10.1088/1361-6641/ac0b94.

[30] R. Gillen, S.J. Clark, J. Robertson, Nature of the electronic band gap in lanthanide oxides, Phys. Rev. B 87 (2013) 125116, https://doi.org/10.1103/PhysRevB.87.125116.

[31] G. Zhou, W. Geng, L. Sun, X. Wang, W. Xiao, J. Wang, L. Wang, Influence of mixed valence on the Formation of oxygen vacancy in cerium oxides, Materials 12 (2019), https://doi.org/10.3390/ma12244041.

[32] H. Unuma, T. Kanehama, K. Yamamoto, K. Watanabe, T. Ogata, M. Sugawara, Preparation of thin films of MnO_2 and CeO_2 by a modified chemical bath (oxidative-soak-coating) method, J. Mater. Sci. 38 (2003) 255–259, https://doi.org/10.1023/A:1021197029004.

[33] K. Timmo, M.D. Sadurni, M. Pilvet, K. Muska, M. Altosaar, V. Mikli, F. Atlan, M. Guc, V. Izquierdo-Roca, M. Grossberg-Kuusk, M. Kauk-Kuusik, Efficiency enhancement of Cu_2ZnSnS_4 monograin layer solar cells via absorber post-growth treatments, Sol. Energy Mater. Sol. Cell. 250 (2023) 112090, https://doi.org/10.1016/J.SOLMAT.2022.112090.

[34] K. Muska, M. Kauk, M. Altosaar, M. Pilvet, M. Grossberg, O. Volobujeva, Synthesis of Cu_2ZnSnS_4 monograin powders with different compositions, Energy Proc. 10 (2011) 203–207, https://doi.org/10.1016/j.egypro.2011.10.178.

[35] K. Timmo, M. Kauk-Kuusik, M. Pilvet, M. Altosaar, M. Grossberg, M. Danilson, R. Kaupmees, V. Mikli, J. Raudoja, T. Varema, $Cu(In,Ga)Se_2$ monograin powders with different Ga content for solar cells, Sol. Energy 176 (2018) 648–655, https://doi.org/10.1016/j.solener.2018.10.078.

[36] K. Timmo, M. Altosaar, M. Pilvet, V. Mikli, M. Grossberg, M. Danilson, T. Raadik, R. Josepson, J. Krustok, M. Kauk-Kuusik, The effect of Ag alloying of $Cu_2(Zn,Cd)SnS_4$ on the monograin powder properties and solar cell performance, J. Mater. Chem. A 7 (2019) 24281–24291, https://doi.org/10.1039/C9TA07768E.

[37] M. Kauk-Kuusik, X. Li, M. Pilvet, K. Timmo, M. Grossberg, T. Raadik, M. Danilson, V. Mikli, M. Altosaar, J. Krustok, J. Raudoja, Study of $Cu_2CdGeSe_4$ monograin powders synthesized by molten salt method for photovoltaic applications, Thin Solid Films 666 (2018) 15–19, https://doi.org/10.1016/j.tsf.2018.09.025.

[38] F. Ghisani, K. Timmo, M. Altosaar, J. Raudoja, V. Mikli, M. Pilvet, M. Kauk-Kuusik, M. Grossberg, Synthesis and characterization of tetrahedrite $Cu_{10}Cd_2Sb_4S_{13}$ monograin material for photovoltaic application, Mater. Sci. Semicond. Process. 110 (2020) 104973, https://doi.org/10.1016/j.mssp.2020.104973.

[39] K. Timmo, M. Pilvet, K. Muska, M. Altosaar, V. Mikli, R. Kaupmees, R. Josepson, J. Krustok, M. Grossberg-Kuusk, M. Kauk-Kuusik, Influence of alkali iodide fluxes on Cu_2ZnSnS_4 monograin powder properties and performance of solar cells, Mater. Adv. 4 (2023) 4509–4519, https://doi.org/10.1039/D3MA00444A.

[40] M. Kauk-Kuusik, K. Timmo, K. Muska, M. Pilvet, J. Ri Krustok, R. Josepson, G. Brammertz, B. Vermang, M. Danilson, M. Grossberg, Detailed Insight into the CZTS/CdS interface modification by air annealing in monograin layer solar cells. https://doi.org/10.1021/acsaem.1c02186, 2021.

[41] M. Kauk-Kuusik, K. Timmo, M. Pilvet, K. Muska, M. Danilson, J. Krustok, R. Josepson, V. Mikli, M. Grossberg-Kuusk, Cu_2ZnSnS_4 monograin layer solar cells for flexible photovoltaic applications, J. Mater. Chem. A 11 (2023) 23640–23652, https://doi.org/10.1039/D3TA04541B.

[42] A. Nasyori, M. Pilvet, A. Saar, J. Krustok, M. Danilson, R. Kaupmees, V. Mikli, Y. Gong, R. Josepson, E. Saucedo, M. Grossberg-Kuusk, M. Kauk-Kuusik, In ambient

air processed Cu_2ZnSnS_4 absorber layers from DMSO-based precursors: enhanced efficiency via device post-annealing, J. Mater. Chem. A 13 (2025) 30167–30179, https://doi.org/10.1039/D5TA04554A.

[43] C. Neubauer, E. Babatas, D. Meissner, Investigation of rough surfaces on $Cu_2ZnSn(S_xSe_{1-x})_4$ monograin layers using light beam induced current measurements, Appl. Surf. Sci. 423 (2017) 465–468, https://doi.org/10.1016/j.apsusc.2017.06.111.

[44] F. Zhang, P. Wang, J. Koberstein, S. Khalid, S.-W. Chan, Cerium oxidation state in ceria nanoparticles studied with X-ray photoelectron spectroscopy and absorption near edge spectroscopy, Surf. Sci. 563 (2004) 74–82, https://doi.org/10.1016/j.susc.2004.05.138.

[45] M.A. Isaacs, C. Drivas, R. Lee, R. Palgrave, C.M.A. Parlett, D.J. Morgan, XPS surface analysis of ceria-based materials: experimental methods and considerations, Appl. Surf. Sci. Adv. 18 (2023) 100469, https://doi.org/10.1016/j.apsadv.2023.100469.

[46] K.I. Maslakov, Y.A. Teterin, A.J. Popel, A.Yu Teterin, K.E. Ivanov, S.N. Kalmykov, V.G. Petrov, P.K. Petrov, I. Farnan, XPS study of ion irradiated and unirradiated CeO_2 bulk and thin film samples, Appl. Surf. Sci. 448 (2018) 154–162, https://doi.org/10.1016/j.apsusc.2018.04.077.

[47] D.J. Morgan, Photoelectron spectroscopy of ceria: reduction, quantification and the myth of the vacancy peak in XPS analysis, Surf. Interface Anal. 55 (2023) 845–850, https://doi.org/10.1002/sia.7254.

[48] R. Saive, S-Shaped current–voltage characteristics in solar cells: a review, IEEE J. Photovolt. 9 (2019) 1477–1484, https://doi.org/10.1109/JPHOTOV.2019.2930409.

[49] B. Ecker, H.-J. Egelhaaf, R. Steim, J. Parisi, E. von Hauff, Understanding S-Shaped current–voltage characteristics in organic solar cells containing a TiO_x interlayer with impedance spectroscopy and equivalent circuit analysis, J. Phys. Chem. C 116 (2012) 16333–16337, https://doi.org/10.1021/jp305206d.